ACS APPLIED MATERIALS & INTERFACES

www.acsami.org

Research Article

Abnormal Phase Transition and Band Renormalization of Guanidinium-Based Organic–Inorganic Hybrid Perovskite

Han Li, Daniel Wines, Bin Chen, Kentaro Yumigeta, Yasir Mohammed Sayyad, Jan Kopaszek, Sui Yang, Can Ataca,* Edward H. Sargent, and Sefaattin Tongay*

Cite This: *ACS Appl. Mater. Interfaces* 2021, 13, 44964–44971

Read Online

ACCESS | Metrics & More | Article Recommendations | Supporting Information

ABSTRACT: Low-dimensional organic–inorganic hybrid perovskites have attracted much interest owing to their superior solar conversion performance, environmental stability, and excitonic properties compared to their three-dimensional (3D) counterparts. Among reduced-dimensional perovskites, guanidinium-based perovskites crystallize in layered one-dimensional (1D) and two-dimensional (2D). Here, our studies demonstrate how the dimensionality of the hybrid perovskite influences the chemical and physical properties under different pressures (i.e., bond distance, angle, vdW distance). Comprehensive studies show that 1D $GuaPbI_3$ does not undergo a phase transition even up to high pressures (~13 GPa) and its band gap monotonically reduces with pressure. In contrast, 2D Gua_2PbI_4 exhibits an early phase transition at 5.5 GPa and its band gap follow nonmonotonic pressure response associated with phase transition as well as other bond angle changes. Computational simulations reveal that the phase transition is related to the structural deformation and rotation of PbI_6 octahedra in 2D Gua_2PbI_4 owing to a larger degree of freedom of deformation. The soft lattice allows them to uptake large pressures, which renders structural phase transitions possible. Overall the results offer the first insights into how layered perovskites with different dimensionality respond to structural changes driven by pressure.

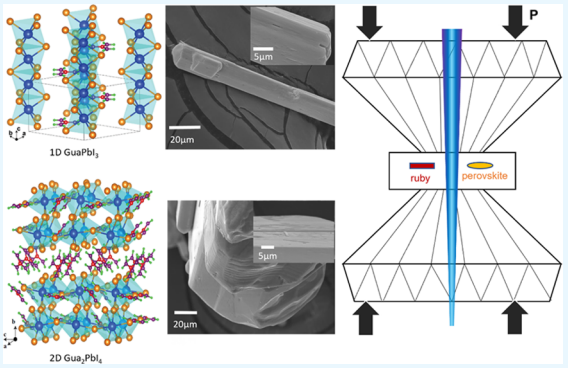

KEYWORDS: *perovskites, layered materials, high pressure, DAC, 2D materials*

INTRODUCTION

The organic–inorganic hybrid halide perovskites have attracted much scientific interest owing to their superior optical properties and promising applications in energy conversion and light-emitting diodes technologies.[1−6] A large number of studies to date have established outstanding three-dimensional (3D) bulk organic–inorganic hybrid perovskites such as $MAPbI_3$, $FAPbI_3$,[7,8] where MA represents $CH_3NH_3^+$ and FA represents $NH_2CH{=}NH_2^+$. These hybrid perovskites exhibit stellar solar efficiencies as new-generation solar cell devices. According to previous studies on crystal synthesis,[9,10] metal halide perovskites may crystallize in the zero-dimensional (0D) to 3D form based on the Goldschmidt tolerance factor,[11] $t = \frac{r_A + r_X}{\sqrt{2}(r_B + r_X)}$, where r_A, r_B, and r_X are the effective radius of cations, metals, and halides. While $0.8 < t < 1$ generally ensures a 3D cubic/tetragonal structure, the cation becomes too large to be contained in 3D structure when $t > 1$. Thus, perovskites form in one-dimensional (1D) ribbons or two-dimensional (2D) layered structures. Because of thermal and moisture instability of 3D hybrid perovskites,[12−14] there is an increasing research effort to the synthesis and application of these low-dimensional organic–inorganic perovskites for higher stability.[15,16] To achieve 1D or 2D nature, organic spacers or larger cations are usually employed to create van der Waals (vdW) gaps. Recent studies have further shown that these low-dimensional counterparts exhibit higher stability, larger exciton binding energy, and longer diffusion length,[17−20] making them ideal candidates for studying intriguing physical properties under high pressures associated with the change of the interatomic distance, bond angles, and lattice constants.

Guanidinium (Gua) is a nonpolar cation and $GuaPbI_3$ has a tolerance factor of 1.03 in the assumed 3D perovskite form. Since the tolerance factor is greater than 1, it crystallizes in the non-3D form. Indeed, the synthesized $GuaPbI_3$ takes the 1D form with face-sharing octahedra, while Gua_2PbI_4 crystallizes in 2Ds with corner-sharing octahedra.[21,22] This enables the Gua-Pb–I system to take different dimensionality with the same type of cation, metal, and halide and thus is a great candidate material system to study the dimensionality and structural transformation effects.

Received: July 31, 2021
Published: September 14, 2021

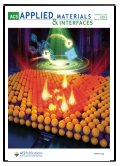

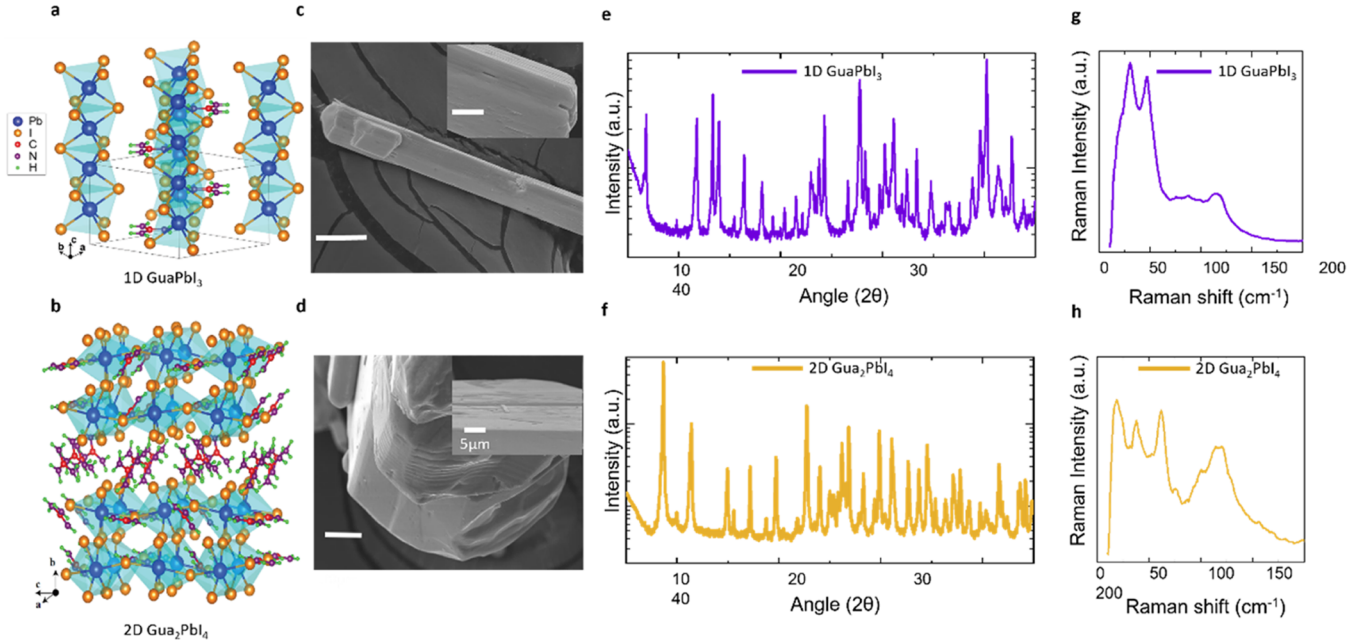

Figure 1. Crystal structure and basic characterization of 1D $GuaPbI_3$ and 2D Gua_2PbI_4. (a, b) Crystal structures of 1D $GuaPbI_3$ and 2D Gua_2PbI_4. (c, d) SEM images of $GuaPbI_3$ and Gua_2PbI_4 (high-resolution SEM image as inset). (e, f) Powder X-ray diffraction of $GuaPbI_3$ and 2D Gua_2PbI_4. (g, h) Raman spectrum of $GuaPbI_3$ and Gua_2PbI_4.

EXPERIMENTAL SECTION

Synthesis of 1D and 2D Guanidinium-Based Perovskites. Lead (II) oxide (PbO, 99.9%), hydroiodic acid (HI, 57% w/w aq), and hydro-phosphorous acid (H_3PO_2, 50% w/w aq) were purchased from Alfa Aesar. Guanidinium carbonate (Gua_2CO_3, 99%) was purchased from Sigma-Aldrich. All chemicals were used without further purification.

$GuaPbI_3$ (1D Ribbon). Five milliliters of HI and 0.1 mL of H_3PO_2 were mixed together in a glass vial. Typically, 144.2 mg of G_2CO_3 (0.8 mmol) was added to the mixture to produce guai. Then, 922.0 mg of PbI_2 (2 mmol) was added in, mixed, and put in an autoclave for hydrothermal synthesis. The reaction temperature was raised in 4 h till 100 °C, kept for 2 h, cooled to 45 °C in 6 h, and further cooled to 25 °C in 8 h.

Gua_2PbI_4 (2D Layers). Five milliliters of HI and 0.1 mL of H_3PO_2 were mixed together in a glass vial. Typically, 540.5 mg of G_2CO_3 (1.5 mmol) was added to the mixture to produce guanidinium iodine (GuaI). Then, 922.0 mg of PbI_2 (2 mmol) was added in, mixed, and put in an autoclave for hydrothermal synthesis. The reaction temperature was raised to 100 °C in 4 h, kept at 100 °C for 2 h, then cooled to 55 °C in 6 h, and further cooled to 25 °C in 8 h.

Theoretical Simulation. Our theoretical calculations were obtained via first-principles pseudopotential calculations that were based on density functional theory (DFT), including spin-orbit coupling (SOC) effects. These calculations were performed within the generalized gradient approximation (GGA), taking into account van der Waals (vdW) corrections, for which we used the DFT-D2[23] method of Grimme. Projector augmented-wave (PAW) potentials were used, and we approximated the exchange-correlation potential using the Perdew–Burke–Ernzerhof (PBE) functional.[24,25] For these numerical calculations, we used the Vienna ab-initio simulation package (VASP).[26] The plane-wave basis set kinetic energy cutoff was chosen to be 500 eV. We used the Monkhorst–Pack scheme[27] with a γ-centered mesh to sample the Brillouin zone using a $6 \times 6 \times 6$ k-point grid for 1D $GuaPbI_3$ and a $4 \times 2 \times 3$ grid for 2D Gua_2PbI_4. To optimize atomic positions at each value of volumetric strain on the lattice, we used the conjugate gradient method, which allowed us to minimize the ground-state energy and atomic forces for each configuration. The starting geometries prior to atomic relaxation for 1D and 2D structures were obtained from ref 22. The convergence requirement between any two steps in the energy optimization procedure was chosen to be 10^{-5} eV. In addition, we used the Gaussian smearing method with a smearing width of 0.02 eV for all density of states calculations. To visualize crystal structures, we used the VESTA software.[28]

In-situ Characterization in a Diamond Anvil Cell. A diamond anvil cell is a device to allow control over pressure. Guanidinium-based perovskites (1D $GuaPbI_3$ and 2D Gua_2PbI_4) were placed in the gasket hole with 0.21 mm diameter. NaCl is used as pressure media to introduce pressure. Ruby is used as a pressure gauge to regulate the pressure. PL spectra were measured with 355 nm UV laser and Raman spectrum were measured with 532 nm green laser in backscattering configuration with 1200/mm grating. The spot size is ~2 μm and laser power is 1.3 mW for Raman and 320 μW for PL measurement. Micro-absorption spectrum was obtained through a home-made spectrometer in backscattering configuration. Tungsten light is used as a light source. The spectrum range is from 400 to 750 nm, and the spot size is around 20 μm.

Optical Characterization. UV–vis absorption spectrum was obtained by a Lambda 950, Perkin-Elmer spectrophotometer. Deuterium and tungsten halogen light are used as the light source for UV and visible. A 5 mm × 5 mm perovskite sample is attached to the aperture. The spectrum range is from 250 to 800 nm, in the step of 2 nm. SEM samples were prepared by drop casting (perovskite samples) directly on a 300 nm oxide thick Si/SiO_2 substrate. The substrate was sonicated with ethanol and IPA to remove any organic contaminants followed by a 15 min Ar plasma treatment. The samples were sputtered with Au/Pd prior to the measurement to make the surface conductive. The thickness of the sputtered film was about 10 nm. SEM and EDX were performed using a Zeiss Auriga FIB-SEM at 20 KV acceleration voltage from a field emission source and collected using a back-scattered electron detector and a 30 μm aperture. The collection bias was maintained at 300 V throughout the measurement. X-ray diffraction was performed on Siemens D5000 with Cu source.

Low-Temperature and Power-Dependent PL Measurement. Our low-temperature and power-dependent PL measurements were carried out in a home-built micro-spectroscopy setup: a cryostat (Janis ST-500) to cool the sample at low temperature with liquid helium flow; the long working distance objective lens (NIKON Plan Fluor ELWD 40×) with a numerical aperture NA of 0.6 and objective correction collars for localizing the samples in the cryostat; and a 2D

https://doi.org/10.1021/acsami.1c14521
ACS Appl. Mater. Interfaces 2021, 13, 44964–44971

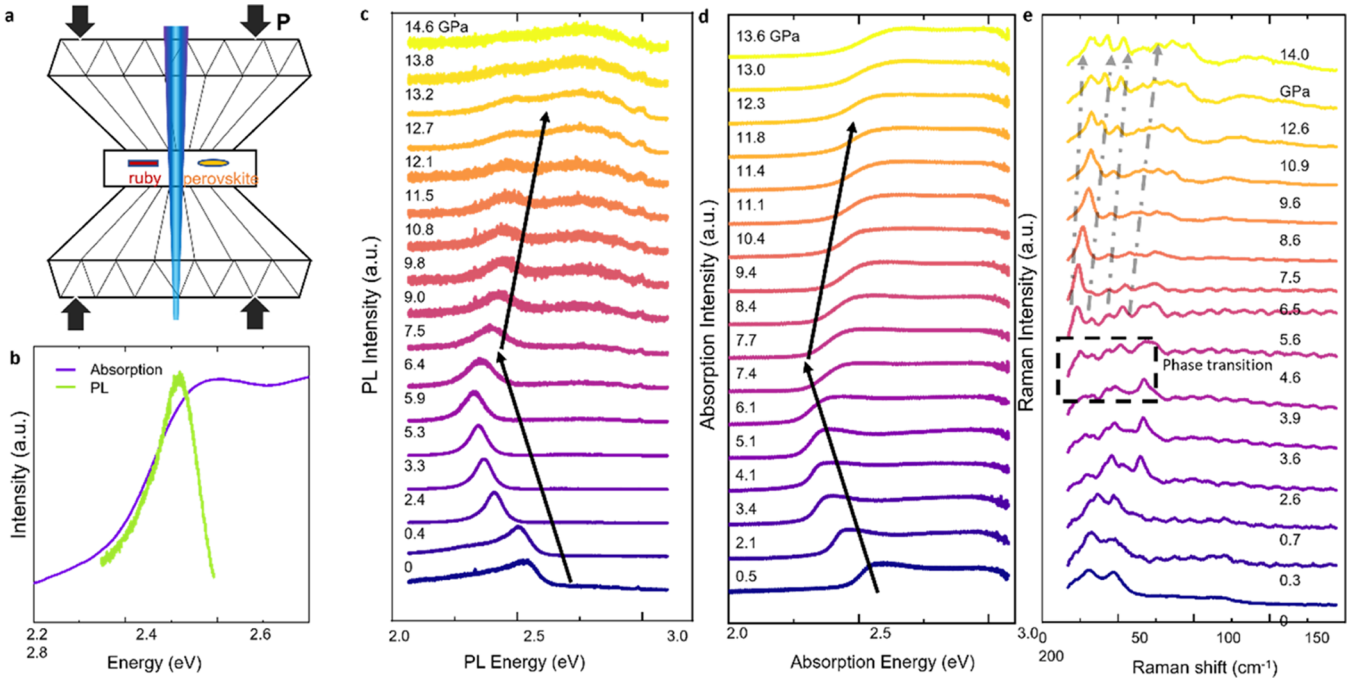

Figure 2. High-pressure studies on 2D Gua_2PbI_4. (a) Schematic of a diamond anvil cell. (b) Photoluminescence and UV−vis absorption spectrum of 2D Gua_2PbI_4. (c−e) Stacking PL, microabsorption, and Raman spectrum of 2D Gua_2PbI_4 at high pressures.

EMCCD array camera with a spectragraph (Andor spectrometer) was used for the signal detection. For the measurements, a continuous-wave laser (473 nm) was used as the pump source. The motorized half-wave plate was used to control the incident power for the power-dependent measurement, and edge filters were put in the detection path to remove any pump signals.

RESULTS AND DISCUSSION

Here, a diamond anvil cell (DAC) allows us to change the interatomic distance, bond angles, and lattice constants on demand by applying high pressures to explore the phase transformation and band renormalization effects. To date, several studies have been carried out for 3D organic halide perovskites and unique phase transition caused by PbX_6 rotation has been reported.[29−31] However, the high-pressure response and origin of phase transition for low-dimensional perovskites, especially the dimensionality (1D vs 2D) effects, are still remain challenging. In this work, we report on the synthesis and optical characterization of pseudo-1D $GuaPbI_3$ ribbons and 2D Gua_2PbI_4 layers and access their high-pressure (up to 15 GPa) behavior using DAC integrated with Raman, photoluminescence (PL), and microabsorption spectroscopy setup. Experimental results together with comprehensive density functional (DFT) simulations first establish how bond angles, distance, and overall octahedra deform under pressure for 1D and 2D perovskites and how the dimensionality influences the phase transition and band renormalization (tuning) effects.

The organic perovskites are synthesized by solution-based methods[32] (see Experimental Section) following established protocols, and the crystal structures of 1D $GuaPbI_3$ and 2D Gua_2PbI_4 are schematically shown in Figure 1a,b. In the 1D case, the PbI_6 octahedra extend and form 1D chain along the *c*-axis direction, wherein these pseudo-1D chains are coupled together through weak vdW forces. On the contrary, the double chain of inorganic PbI_3^- are separated by Gua (guanidinium) cations[22] to form 2D layers (lattice), which are stacked along the *b*-axis again coupled through vdW forces much similar to inorganic vdW crystals such as graphite, MoS_2, and others. The scanning electron microscopy (SEM) image of 1D $GuaPbI_3$ and 2D Gua_2PbI_4 (Figure 1d) highlights the 1D and 2D vdW nature of these as-synthesized layers. The XRD spectra collected from 1D $GuaPbI_3$ and 2D Gua_2PbI_4 match well with the previously reported work.[22] Finally, the Raman spectroscopy spectra of 1D $GuaPbI_3$ and 2D Gua_2PbI_4 obtained at ambient pressure exhibit three prominent low-frequency peaks at 26, 37, and 58 cm^{-1} for $GuaPbI_3$ and four peaks located at 27, 35, 46, and 57 cm^{-1} for 2D Gua_2PbI_4. These low-frequency Raman peaks can be attributed to zone-folded LA phonons or optical modes.[33]

We start our discussions on the high-pressure behavior of these vdW halides with 2D Gua_2PbI_4. To investigate the pressure dependence of guanidinium-based perovskites, we applied pressures (0−15 GPa) on 2D Gua_2PbI_4 and carried out photoluminescence and microabsorption measurements under different applied pressures. 2D Gua_2PbI_4 thin flake (lateral size ∼100 μm and thickness ∼50 nm) was exfoliated from as-grown crystals and transferred into DAC (see the schematic in Figure 2a). Standard ruby fluorescence was used as the pressure gauge to determine the pressure inside the DAC chamber.[34] We also note that sodium chloride is highly preferred over methanol/ethanol media to eliminate the possibility of chemical reactions between perovskites and pressure transmitting media. In all of the measurements, the behavior was monitored both during compression and decompression to ensure that the results are accurate and are fully reversible.

Under ambient pressure, in Figure 2b, photoluminescence (PL) peaks and UV−vis absorption show strong absorption at 2.5 and 2.55 eV, respectively. To extract out the band gap from the UV−vis absorption spectrum, we use direct band fitting[35] $(\alpha h\nu)^2 = C(E_g - h\nu)$, in which α is absorption coefficient, $h\nu$ is the energy, C is the material depending constant, and E_g is the

https://doi.org/10.1021/acsami.1c14521
ACS Appl. Mater. Interfaces 2021, 13, 44964−44971

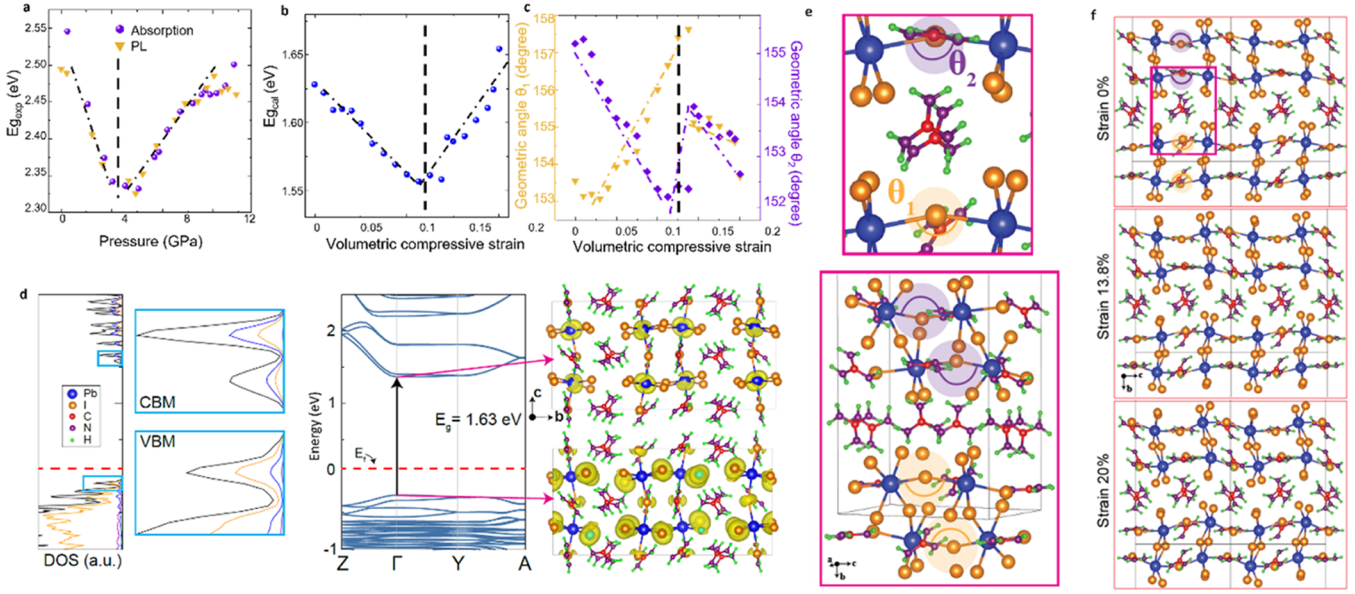

Figure 3. DFT simulation of band tuning and change of a geometry angle. (a) Experimental band gap extracted from microabsorption and PL. (b, c) Simulated band gap tuning and the corresponding geometric angle under volumetric strain. (d) Simulated density of states, band structure, and orbit contribution of 2D Gua_2PbI_4. (e) Schematic of angles θ_1 and θ_2. (f) Crystal structures and angle changing of Gua_2PbI_4 at different strains.

band gap of the material. The extrapolation result shows that the band gap from the UV−vis spectrum locates at 2.5 eV, which matches well with the PL data. We also note that the energy difference (50 meV) between the PL peak (2.50 eV) at absorption increase (2.55 eV) is related to the Stokes shift phenomena as previously discussed in the literature.[36]

We find that the 2D Gua_2PbI_4 band gap has an unusual pressure response. The prominent PL peak first red-shifts from 2.50 to 2.34 eV at a rate of −28.3 meV/GPa (Figure 2c). This red shift response with pressure is usually observed in conventional material systems such as porous silicon, As_2S_3, GaAs, 2D ReS_2, $ReSe_2$, and other traditional semiconductors.[37−40] Further applied pressure above 5.9 GPa causes PL emission from 2D Gua_2PbI_4 to blue shift from 2.34 to 2.45 eV as the pressure increases from 5.9 to 9.8 GPa (+30.8 meV/GPa) and remains nearly constant from 10.8 to 13.8 GPa with a minuscule change from 2.45 to 2.46 eV.

Microabsorption measurement, a more direct gauge of band gap values, at different pressures (Figure 2d) agrees well with the PL response. Similar to trends in Figure 2c, the band gap extracted from the microabsorption spectra first red-shifts (up to 5.1 GPa from 2.55 to 2.33 eV, rate: −47.8 meV/GPa) followed with blue shift in the band gap (from 2.32 to 2.45 eV with a rate of 30.2 meV/GPa in the 6.1−10.4 GPa range), and finalized with the pressure-independent regime from 11.1 to 13.6 GPa with small band gap change (2.46−2.50 eV). The summarized values from PL and microabsorption studies show remarkable agreement, as shown in Figure 3a. We also note that the onset at which this unusual reversal behavior is observed (5.9 GPa) coincides well with the sudden change in the Raman spectra shown in Figure 2e. To be more specific, starting from 3.7 GPa, a new peak emerges at 25 cm^{-1} and becomes dominant with compression. Before the transition, there are three peaks located at 45, 52, and 64 cm^{-1}; after the transition, there are four major peaks located at 25, 43, 54, and 74 cm^{-1}. All of the peaks are stiffening with increasing pressure. This suggests that the observed behavior might be associated with the pressure-induced phase transformation, as depicted in Figure 2d.

To understand the origin of the pressure-induced structural phase transition and band gap variation in 2D Gua_2PbI_4 layers, we performed comprehensive DFT calculations including the spin-orbit coupling (SOC) correction. Since the unit cell involves a large number of atoms, we present the total density of states (DOS), atomic projected DOS (PDOS), as well as the orbital contribution at the valence band maximum (VBM) and conduction band minimum (CBM) in Figure 3d. We note that SOC-included DFT (1.63 eV direct band gap at the Γ point) underestimates the band gap compared to experimental values (2.5 eV). Here, the atomic contribution at the VBM is mostly coming from iodine 5p (overlap of p_x, p_y, p_z) orbitals, whereas the 6p (mostly p_z with a small overlap from p_x and p_y) orbitals of Pb contribute to the CBM position.

To mimic high pressure, volumetric compressive strain was applied to the lattice (decreased *a*, *b*, and *c* by an equal amount). Atomic positions and lattice vectors were allowed to relax while keeping the volume constant at each strain value for up to 20% strain with ∼1% strain increments, as shown in Figure 3b. Similarly to the experimental data (Figure 3a), theory predictions show that the band gap does not linearly red-shift, but instead, the trend suddenly reverses at a critical strain value (∼13%), as depicted in Figure 3b (see details in Figure S1). Although DFT band gaps are significantly lower than the measured values, which are due to the DFT approximations used (GGA functional which systematically underestimates the band gap), overall trends are in great agreement with measured band gap trends.

Interpreting these nonmonotonic trends requires a detailed understanding of how the 2D Gua_2PbI_4 structure changes with pressure and how such change influences its electronic behavior. Here, we first define two critical angles θ_1 and θ_2 in the 2D Gua_2PbI_4 unit cell (Figure 3e). The 2D (unstrained) structure consists of Pb−I chains that are oriented along the c-axis and chain angles (θ_1 and θ_2) have a mirror symmetry about the [010] plane. θ_1 represents the Pb−I−Pb angle of the

https://doi.org/10.1021/acsami.1c14521
ACS Appl. Mater. Interfaces 2021, 13, 44964−44971

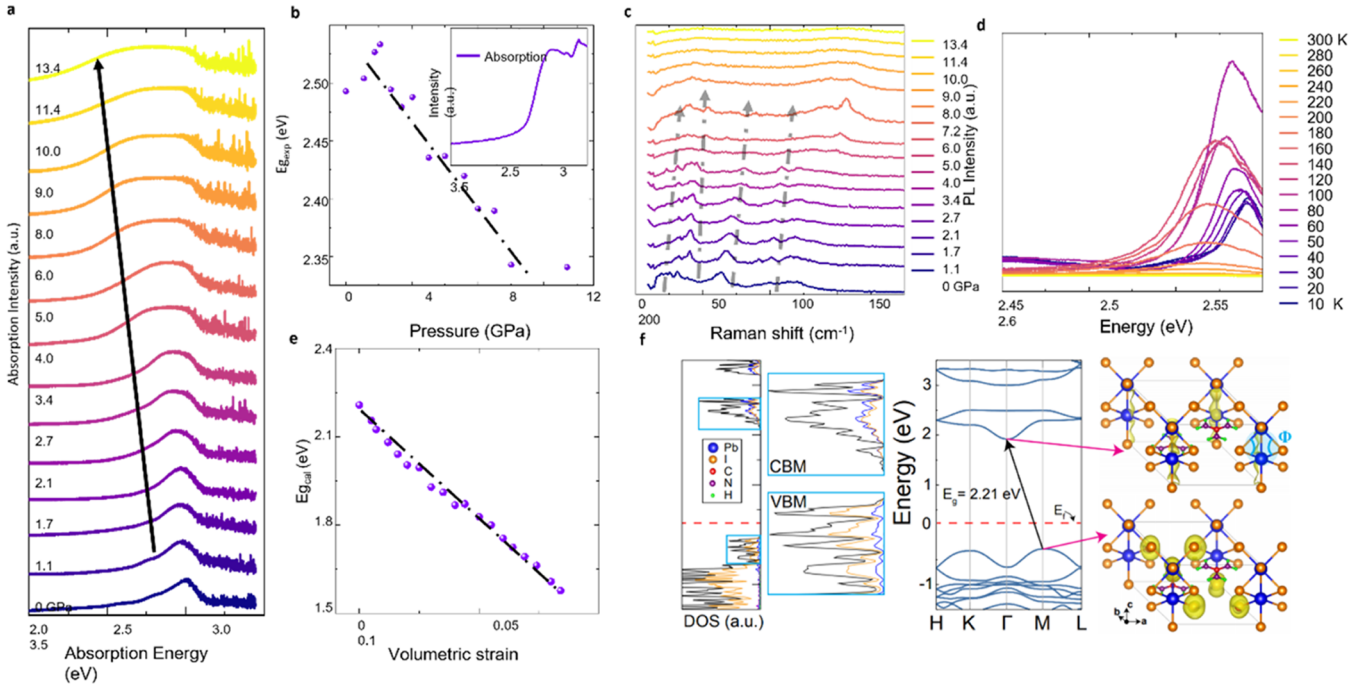

Figure 4. High-pressure studies on 1D $GuaPbI_3$. (a) Stacking plot of microabsorption spectrum from 0 to 13.4 GPa. (b) Extracted band gap from microabsorption versus pressure and UV−vis absorption spectrum as the intersection. (c) Stacking plot of Raman spectrum from 0 to 13.4 GPa. (d) Stacking plot of low-temperature PL spectrum from 10 to 300 K. (e) Calculated band gap at different volumetric strains. (f) Simulated DOS, band structure, and orbit contribution of VBM and CBM; the angles of Pb−I−Pb are highlighted in cyan.

outside chains, while θ_2 represents the angle of the inside chains within the 2D structure. Figure 3c depicts how θ_1 and θ_2 change as volumetric strain increases. Up until ∼13% strain, their response to pressure shows an opposite trend in that θ_1 increases and θ_2 decreases linearly. Above ∼13% strain, these two bond angles show a sudden jump in their values, which suggests a structural phase transition as experimentally observed within our Raman spectroscopy studies (Figure 2e). After this point, the [010] symmetry is broken in the structure and neighbor chains begin to rotate counterclockwise about the *c*-axis up until 20% strain, as shown in Figure 3f.

The variation of the band gap can best be explained by how the 6p orbitals of Pb and 5p and of I interact with each other when θ_1 and θ_2 simultaneously change during atomic relaxation, which tunes VBM and CBM levels. As volumetric strain is applied, the VBM and CBM are shifted simultaneously due to the interaction of these orbitals induced by structural distortion. From 0% strain to 13.8% strain, the VBM decreases by 0.05 eV while the CBM decreases by 0.12 eV, which results in a net band gap decrease of 0.07 eV. This is primarily due to shorter Pb−I distances (a 3% reduction in Pb−I distance from 0 to 13.8% strain), which increases the interaction between 5p orbitals of I and 6p of Pb. As additional strain is applied after the change to the high-pressure phase (16.3−19.4%), the VBM decreases by 0.055 eV while the CBM decreases by 0.02 eV, resulting in a net 0.035 eV band gap increase. In addition to changes in θ_1 and θ_2, the dominant VBM change can be best explained by how interchain distances change as strain is applied. From Figure S2, we observe that as strain is applied, the interchain (Pb−Pb and I−I distances) distances both decrease. After the high-pressure phase is reached, the I−I distance decreases at a significantly faster rate than the Pb−Pb distance, which causes increased interaction of 5p I orbitals, which drive the VBM down (see the Supporting Information for more details).

How does the dimensionality influence the overall pressure behavior of these guanidinium-based halide perovskites? To gain a deeper understanding, we investigated the pseudo-1D guanidinium lead iodide $GuaPbI_3$, which has the same type of cations, metals, and halides but different chemical compositions due to reduced dimensionality. Instead of 2D stacking across Gua_2PbI_4 layers, PbI_6 octahedra extend along the *c*-axis and forms 1D ribbons. Interestingly, our DAC measurements performed on these 1D $GuaPbI_3$ show that the band gap monotonically red-shifts with pressure as determined from the pressure-dependent microabsorption studies (Figure 4a). The extracted band gap versus pressure is plotted in Figure 4b, wherein the band gap reduces from 2.50 eV at 0 GPa to 2.34 eV at 13.4 GPa with a rate of 11.9 meV/GPa. The UV−vis absorption spectrum at ambient pressure is intersected in Figure 4b and shows a band gap of 2.51 eV, quantitatively matching with microabsorption data. We also note that Raman studies show that there is no noticeable phase transition with pressure as evidenced from retained Raman spectra and symmetry with pressure in Figure 4c. From 0 to 7.2 GPa, four predominant Raman modes are stiffening (shifts to high frequencies) and no evidence of phase transition is observed until all Raman peaks become unmeasurably weak.

It is noteworthy to mention that our studies on 1D $GuaPbI_3$ are mainly based on microabsorption, Raman, and theory simulation since the PL spectrum is unnoticeable at room temperature and prevents us from collecting any pressure-dependent PL spectra. Our theory simulations (Figure 4e) reveal that 1D $GuaPbI_3$ exhibits an indirect band gap, which can partially justify the lack of PL signal. More concrete reasoning for the lack of the PL signal can be clearly seen from the cryogenic PL studies in Figure 4d. It clearly shows that the

https://doi.org/10.1021/acsami.1c14521
ACS Appl. Mater. Interfaces 2021, 13, 44964−44971

PL intensity from 1D $GuaPbI_3$ becomes more efficient (brighter) at low temperatures, which suggests that phonons in 1D $GuaPbI_3$ are more active (due to constriction in 1Ds) in shunting the radiative recombination and promoting the nonradiative process (see Figures S3 and S4).

Overall findings can be well explained by the theoretical insights; DFT results first confirm that the 1D structure is an indirect semiconductor with M → Γ band gap of 2.21 eV. In contrast to the 2D case, the atomic contribution at the VBM is mostly coming from 5p orbitals of I (mostly p_x and p_y) atoms and the contribution at the CBM is coming mostly from $6p_z$ orbitals of Pb atoms. Since 1D $GuaPbI_3$ consists of isolated chains, we applied strain along the *c*-axis direction while relaxing atoms in other directions while keeping the cell shape fixed. Following this protocol, we further relaxed the structure by allowing the cell shape and atomic positions to change while keeping the total volume of the 1D structure fixed. Our DFT results show that the band gap decreases with pressure at a rate of 74 meV/% strain, which is in excellent agreement with the experimental results (see details in Figure S5). This monotonic reduction in the gap values can be attributed to the structural changes in each isolated chain. We observe that the Pb−I−Pb angle (see in Figure 4f) decreases linearly as a function of strain, measuring 71° at 0% strain and reducing to 66.8° after 8%. Such reduction in the Pb−I−Pb angle primarily changes the interaction of 5p orbitals of I and $6p_z$ orbitals of Pb. It is important to note that during volumetric relaxation, the change in volume is dominated by the compression of the *c*-axis, not the change in the *a* or *b*-axis. This means that as the *c*-axis is compressed, the $6p_z$ orbitals of Pb located at the CBM become closer together and create a more significant interaction. In contrast, the change in interchain distances (*a* or *b*-axis) and therefore the distances between corresponding 5p orbitals of I at the VBM are smaller, resulting in 5p orbitals experiencing less of an overall interaction. This is confirmed by the Pb−I bond distances, which do not change significantly as strain is applied (Pb−I bond length: 3.26028 Å at 0% strain and 3.24118 Å at 10% strain). This is a possible explanation of why the CBM value monotonically decreases with applied strain, while the VBM value remains nearly constant. The combination of reduction in CBM values and pressure-independent VBM subsequently results in a reduction in the band gap with pressure as revealed from high-pressure DAC studies.

CONCLUSIONS

Our high-pressure studies on guanidinium-based 1D and 2D halide perovskites highlighted an unusual pressure response arising from dimensionality effects. These studies conclusively show that added degree of freedom in 2D Gua_2PbI_4 results in a phase transition and subsequent abnormal band renormalization. In reduced dimensions, 1D $GuaPbI_3$ does not experience any phase transition and instead exhibit monotonic decrease in the band gap. Together with theory simulation, our experimental work establishes how these unique 1D and 2D halide perovskite systems respond to pressure through comprehensive spectroscopy experiments and first-principles simulations, the fundamental understanding of their band structure, leading to potential in a pressure-sensitive device and discovering new phases.

ASSOCIATED CONTENT

Supporting Information

The Supporting Information is available free of charge at https://pubs.acs.org/doi/10.1021/acsami.1c14521.

Simulated band structures and bond length of Pb−Pb, I−I of 2D Gua_2PbI_4 at different volumetric strains, low-temperature photoluminescence of 1D $GuaPbI_3$, power-dependent photoluminescence of 1D $GuaPbI_3$, and simulated band structures of 1D $GuaPbI_3$ at different volumetric strains (PDF)

AUTHOR INFORMATION

Corresponding Authors

Can Ataca − *Department of Physics, University of Maryland, Baltimore County, Baltimore, Maryland 21250, United States;* orcid.org/0000-0003-4959-1334; Email: ataca@umbc.edu

Sefaattin Tongay − *Materials Science and Engineering, School for Engineering of Matter, Transport and Energy, Arizona State University, Tempe, Arizona 85287, United States;* orcid.org/0000-0001-8294-984X; Email: Sefaattin.tongay@asu.edu

Authors

Han Li − *Materials Science and Engineering, School for Engineering of Matter, Transport and Energy, Arizona State University, Tempe, Arizona 85287, United States*

Daniel Wines − *Department of Physics, University of Maryland, Baltimore County, Baltimore, Maryland 21250, United States;* orcid.org/0000-0003-3855-3754

Bin Chen − *Department of Electrical and Computer Engineering, University of Toronto, Toronto, Ontario M5S 1A1, Canada*

Kentaro Yumigeta − *Materials Science and Engineering, School for Engineering of Matter, Transport and Energy, Arizona State University, Tempe, Arizona 85287, United States*

Yasir Mohammed Sayyad − *Materials Science and Engineering, School for Engineering of Matter, Transport and Energy, Arizona State University, Tempe, Arizona 85287, United States*

Jan Kopaszek − *Materials Science and Engineering, School for Engineering of Matter, Transport and Energy, Arizona State University, Tempe, Arizona 85287, United States*

Sui Yang − *Department of Physics, University of Maryland, Baltimore County, Baltimore, Maryland 21250, United States*

Edward H. Sargent − *Department of Electrical and Computer Engineering, University of Toronto, Toronto, Ontario M5S 1A1, Canada;* orcid.org/0000-0003-0396-6495

Complete contact information is available at: https://pubs.acs.org/10.1021/acsami.1c14521

Notes

The authors declare no competing financial interest.

ACKNOWLEDGMENTS

The authors acknowledge the use of facilities within the Eyring Materials Center at Arizona State University supported in part by NNCI-ECCS-1542160. Funding for the computational portion of this work was provided by the National Science Foundation through the Division of Materials Research under

NSF DMR-1726213. S.T. acknowledges the support for synthesis efforts (NSF CMMI-182559 and CMMI-1933214), electrical characterization (ECCS 2052527), and excitonic characterization (DMR-2111812). S.Y. acknowledges ASU start-up fund and helpful discussion from Xiang Zhang at UC Berkeley.

REFERENCES

(1) Zhao, Y.; Zhu, K. Organic−Inorganic Hybrid Lead Halide Perovskites for Optoelectronic and Electronic Applications. *Chem. Soc. Rev.* **2016**, *45*, 655−689.
(2) Chen, Q.; De Marco, N.; Yang, Y. M.; Song, T.-B.; Chen, C.-C.; Zhao, H.; Hong, Z.; Zhou, H.; Yang, Y. Under the Spotlight: The Organic−Inorganic Hybrid Halide Perovskite for Optoelectronic Applications. *Nano Today* **2015**, *10*, 355−396.
(3) Fu, H. Review of Lead-Free Halide Perovskites as Light-Absorbers for Photovoltaic Applications: From Materials to Solar Cells. *Sol. Energy Mater. Sol. Cells* **2019**, *193*, 107−132.
(4) Ha, S. T.; Liu, X.; Zhang, Q.; Giovanni, D.; Sum, T. C.; Xiong, Q. Synthesis of Organic−Inorganic Lead Halide Perovskite Nanoplatelets: Towards High-Performance Perovskite Solar Cells and Optoelectronic Devices. *Adv. Opt. Mater.* **2014**, *2*, 838−844.
(5) Byun, J.; Cho, H.; Wolf, C.; Jang, M.; Sadhanala, A.; Friend, R. H.; Yang, H.; Lee, T. W. Efficient Visible Quasi-2D Perovskite Light-Emitting Diodes. *Adv. Mater.* **2016**, *28*, 7515−7520.
(6) Wang, H. C.; Bao, Z.; Tsai, H. Y.; Tang, A. C.; Liu, R. S. Perovskite Quantum Dots and Their Application in Light-Emitting Diodes. *Small* **2018**, *14*, No. 1702433.
(7) Yang, M.; Zhou, Y.; Zeng, Y.; Jiang, C. S.; Padture, N. P.; Zhu, K. Square-Centimeter Solution-Processed Planar CH3NH3PbI3 Perovskite Solar Cells with Efficiency Exceeding 15%. *Adv. Mater.* **2015**, *27*, 6363−6370.
(8) Zhang, Y.; Seo, S.; Lim, S. Y.; Kim, Y.; Kim, S.-G.; Lee, D.-K.; Lee, S.-H.; Shin, H.; Cheong, H.; Park, N.-G. Achieving Reproducible and High-Efficiency (>21%) Perovskite Solar Cells with a Presynthesized FAPbI3 Powder. *ACS Energy Lett.* **2020**, *5*, 360−366.
(9) Jodlowski, A. D.; Yépez, A.; Luque, R.; Camacho, L.; De Miguel, G. Benign-By-Design Solventless Mechanochemical Synthesis of Three-, Two-, and One-Dimensional Hybrid Perovskites. *Angew. Chem., Int. Ed.* **2016**, *55*, 14972−14977.
(10) Lin, H.; Zhou, C.; Tian, Y.; Siegrist, T.; Ma, B. Low-Dimensional Organometal Halide Perovskites. *ACS Energy Lett.* **2018**, *3*, 54−62.
(11) Fu, Y.; Hautzinger, M. P.; Luo, Z.; Wang, F.; Pan, D.; Aristov, M. M.; Guzei, I. A.; Pan, A.; Zhu, X.; Jin, S. Incorporating Large A Cations into Lead Iodide Perovskite Cages: Relaxed Goldschmidt Tolerance Factor and Impact on Exciton−Phonon Interaction. *ACS Cent. Sci.* **2019**, *5*, 1377−1386.
(12) Senocrate, A.; Kim, G. Y.; Grätzel, M.; Maier, J. Thermochemical Stability of Hybrid Halide Perovskites. *ACS Energy Lett.* **2019**, *4*, 2859−2870.
(13) Xu, K. J.; Wang, R. T.; Xu, A. F.; Chen, J. Y.; Xu, G. Hysteresis and Instability Predicted in Moisture Degradation of Perovskite Solar Cells. *ACS Appl. Mater. Interfaces* **2020**, *12*, 48882−48889.
(14) Li, Z.; Liu, N.; Meng, K.; Liu, Z.; Hu, Y.; Xu, Q.; Wang, X.; Li, S.; Cheng, L.; Chen, G. A New Organic Interlayer Spacer for Stable and Efficient 2D Ruddlesden−Popper Perovskite Solar Cells. *Nano Lett.* **2019**, *19*, 5237−5245.
(15) Liang, C.; Gu, H.; Xia, Y.; Wang, Z.; Liu, X.; Xia, J.; Zuo, S.; Hu, Y.; Gao, X.; Hui, W.; et al. Two-Dimensional Ruddlesden−Popper Layered Perovskite Solar Cells Based on Phase-Pure Thin Films. *Nat. Energy* **2021**, *6*, 38−45.
(16) Jang, Y.-W.; Lee, S.; Yeom, K. M.; Jeong, K.; Choi, K.; Choi, M.; Noh, J. H. Intact 2D/3D Halide Junction Perovskite Solar Cells via Solid-phase in-plane Growth. *Nat. Energy* **2021**, *6*, 63−71.
(17) Deng, S.; Shi, E.; Yuan, L.; Jin, L.; Dou, L.; Huang, L. Long-Range Exciton Transport and Slow Annihilation in Two-Dimensional Hybrid Perovskites. *Nat. Commun.* **2020**, *11*, No. 664.
(18) Wang, M.; Zou, H.; Zhang, J.; Wu, T.; Xu, H.; Haacke, S.; Hu, B. Extremely Long Spin Lifetime of Light-Emitting States in Quasi-2D Perovskites Through Orbit−Orbit Interaction. *J. Phys. Chem. Lett.* **2020**, *11*, 3647−3652.
(19) Zhao, C.; Tian, W.; Sun, Q.; Yin, Z.; Leng, J.; Wang, S.; Liu, J.; Wu, K.; Jin, S. Trap-Enabled Long-Distance Carrier Transport in Perovskite Quantum Wells. *J. Am. Chem. Soc.* **2020**, *142*, 15091−15097.
(20) Lee, J.-W.; Dai, Z.; Han, T.-H.; Choi, C.; Chang, S.-Y.; Lee, S.-J.; De Marco, N.; Zhao, H.; Sun, P.; Huang, Y. 2D Perovskite Stabilized Phase-pure Formamidinium Perovskite Solar Cells. *Nat. Commun.* **2018**, *9*, No. 3021.
(21) Jodlowski, A. D.; Roldán-Carmona, C.; Grancini, G.; Salado, M.; Ralaiarisoa, M.; Ahmad, S.; Koch, N.; Camacho, L.; De Miguel, G.; Nazeeruddin, M. K. Large Guanidinium Cation Mixed with Methylammonium in Lead Iodide Perovskites for 19% Efficient Solar Cells. *Nat. Energy* **2017**, *2*, 972−979.
(22) Deng, Z.; Kieslich, G.; Bristowe, P. D.; Cheetham, A. K.; Sun, S. Octahedral Connectivity and Its Role in Determining the Phase Stabilities and Electronic Structures of Low-Dimensional, Perovskite-Related Iodoplumbates. *APL Mater.* **2018**, *6*, No. 114202.
(23) Grimme, S. Semiempirical GGA-Type Density Functional Constructed with a Long-Range Dispersion Correction. *J. Comput. Chem.* **2006**, *27*, 1787−1799.
(24) Blöchl, P. E. Projector Augmented-Wave Method. *Phys. Rev. B* **1994**, *50*, No. 17953.
(25) Perdew, J. P.; Burke, K.; Ernzerhof, M. Generalized Gradient Approximation Made Simple. *Phys. Rev. Lett.* **1996**, *77*, No. 3865.
(26) Kresse, G.; Furthmüller, J. Efficient Iterative Schemes for Ab Initio Total-Energy Calculations Using a Plane-wave Basis Set. *Phys. Rev. B* **1996**, *54*, No. 11169.
(27) Monkhorst, H. J.; Pack, J. D. Special Points for Brillouin-Zone Integrations. *Phys. Rev. B* **1976**, *13*, No. 5188.
(28) Momma, K.; Izumi, F. VESTA 3 for Three-Dimensional Visualization of Crystal, Volumetric and Morphology Data. *J. Appl. Crystallogr.* **2011**, *44*, 1272−1276.
(29) Wang, L.; Wang, K.; Zou, B. Pressure-Induced Structural and Optical Properties of Organometal Halide Perovskite-Based Formamidinium Lead Bromide. *J. Phys. Chem. Lett.* **2016**, *7*, 2556−2562.
(30) Yin, T.; Fang, Y.; Chong, W. K.; Ming, K. T.; Jiang, S.; Li, X.; Kuo, J. L.; Fang, J.; Sum, T. C.; White, T. J.; et al. High-Pressure-Induced Comminution and Recrystallization of CH3NH3PbBr3 Nanocrystals as Large Thin Nanoplates. *Adv. Mater.* **2018**, *30*, No. 1705017.
(31) Lee, J.-H.; Bristowe, N. C.; Lee, J. H.; Lee, S.-H.; Bristowe, P. D.; Cheetham, A. K.; Jang, H. M. Resolving the Physical Origin of Octahedral Tilting in Halide Perovskites. *Chem. Mater.* **2016**, *28*, 4259−4266.
(32) Daub, M.; Haber, C.; Hillebrecht, H. Synthesis, Crystal Structures, Optical Properties, and Phase Transitions of The Layered Guanidinium-Based Hybrid Perovskites [C(NH2)3]2MI4; M = Sn, Pb. *Eur. J. Inorg. Chem.* **2017**, *2017*, 1120−1126.
(33) Dahod, N. S.; France-Lanord, A.; Paritmongkol, W.; Grossman, J. C.; Tisdale, W. A. Low-Frequency Raman Spectrum of 2D Layered Perovskites: Local Atomistic Motion or Superlattice Modes? *J. Chem. Phys.* **2020**, *153*, No. 044710.
(34) Mao, H.; Xu, J.-A.; Bell, P. Calibration of The Ruby Pressure Gauge to 800 Kbar Under Quasi-Hydrostatic Conditions. *J. Geophys. Res.* **1986**, *91*, 4673−4676.
(35) Ghobadi, N. Band Gap Determination Using Absorption Spectrum Fitting Procedure. *Int. Nano Lett.* **2013**, *3*, No. 2.
(36) Brennan, M. C.; Zinna, J.; Kuno, M. Existence of a Size-Dependent Stokes Shift in CsPbBr3 Perovskite Nanocrystals. *ACS Energy Lett.* **2017**, *2*, 1487−1488.
(37) Sood, A.; Jayaram, K.; Muthu, D. V. S. Raman and High-Pressure Photoluminescence Studies On Porous Silicon. *J. Appl. Phys.* **1992**, *72*, 4963−4965.
(38) Wang, J.; Wu, B.; Zhang, G.; Tian, L.; Gu, G.; Gao, C. Pressure Induced Semiconductor−Metal Phase Transition in Gaas: Exper-

imental and Theoretical Approaches. *RSC Adv.* **2016**, *6*, 10144−10149.
(39) Besson, J.; Cernogora, J.; Zallen, R. Effect of Pressure On Optical Properties of Crystalline As_2S_3. *Phys. Rev. B* **1980**, *22*, No. 3866.
(40) Oliva, R.; Laurien, M.; Dybala, F.; Kopaczek, J.; Qin, Y.; Tongay, S.; Rubel, O.; Kudrawiec, R. Pressure Dependence of Direct Optical Transitions in ReS_2 and $ReSe_2$. *npj 2D Mater. Appl.* **2019**, *3*, No. 20.

https://doi.org/10.1021/acsami.1c14521
ACS Appl. Mater. Interfaces 2021, 13, 44964−44971